Ore Geology Reviews 101 (2018) 165–179

Contents lists available at ScienceDirect

Ore Geology Reviews

journal homepage: www.elsevier.com/locate/oregeorev

Using integrated *in-situ* sulfide trace element geochemistry and sulfur isotopes to trace ore-forming fluids: Example from the Mina Justa IOCG deposit (southern Perú)

Rucao Li[a], Huayong Chen[a,b,*], Xiaoping Xia[c,*], Qing Yang[c], Leonid V. Danyushevsky[d], Chunkit Lai[d,e]

[a] Key Laboratory of Mineralogy and Metallogeny, Guangzhou Institute of Geochemistry, Chinese Academy of Sciences, Guangzhou 510604, China
[b] State Key Laboratory of Ore Deposit Geochemistry, Institute of Geochemistry, Chinese Academy of Sciences, Guiyang 550002, China
[c] State Key Laboratory of Isotope Geochemistry, Guangzhou Institute of Geochemistry, Chinese Academy of Sciences, Guangzhou 510604, China
[d] ARC Centre for Excellence in Ore Deposits (CODES), University of Tasmania, Hobart 7001, Australia
[e] Faculty of Science, University Brunei Darussalam, Gadong BE1410, Brunei Darussalam

ARTICLE INFO

Keywords:
Mina Justa IOCG deposit
In-situ sulfur isotopes
Sulfide trace element
External fluids
Perú

ABSTRACT

The Cretaceous Mina Justa iron oxide copper-gold (IOCG) deposit in southern Perú is an important deposit in the Central Andean IOCG mineralization belt. At Mina Justa, Stage I alteration is represented by albite-actinolite, followed by Stage II K-feldspar-magnetite alteration. Stage III alteration is composed mainly of prismatic actinolite, and Stage IV of specular hematite. *In-situ* SIMS sulfur isotope and LA-ICP-MS trace element analyses were conducted on the major sulfide phases, i.e., pyrite from the magnetite-pyrite-K-feldspar alteration (Stage V) and chalcopyrite from the Cu mineralization (Stage VI). Results show that the $\delta^{34}S$ values of Stage V pyrite range from −0.5 to +6.4‰, indicating that the sulfur is mainly magmatic and has possible late external fluid incursion. Co/Ni (0.1 to 209) and Se/S (0.3 to 1.4×10^{-4}) ratios show clear coupling with the $\delta^{34}S$ values, which is also indicative of external fluid incursion during Stage V pyrite formation. Two distinct fluid sources were identified for Stage V: One shows magmatic affinity with low $\delta^{34}S$ (< +2.5‰) and Co/Ni (< 1) but high Se/S (1.2 to 1.4×10^{-4}), and the other shows non-magmatic fluid (e.g., basinal brine) affinity with high $\delta^{34}S$ (> +2.5‰, up to +6.4‰) and Co/Ni (> 10, up to 209) but low Se/S (as low as 0.3×10^{-4}). The Stage VI chalcopyrite grains that did not replace Stage V pyrite have $\delta^{34}S$ values clustering around +1.0‰, suggestive of a magmatic-like origin. Given the low homogenization temperature of fluid inclusions (~88 to 220 °C, mode ~130 °C) and Ca-rich nature of the fluids in Stage VI, the ore-forming materials may have derived from the andesitic host rocks, although derivation via mixing with magmatic fluids may have also been possible. For the Stage VI chalcopyrite grains that replaced Stage V pyrite, both their $\delta^{34}S$ values and trace element patterns show inheritance of the replaced pyrite. In summary, Stage V ore-forming fluids was likely magmatic initially, with external fluid incursion occurring later in this stage; whereas the fluids of Cu mineralization stage may have come mainly from the external fluids that leached the andesitic wall rocks, during which the external fluids had inherited certain sulfur isotope and trace element signatures of the pyrite they replaced.

1. Introduction

Sulfide minerals are present in many types of mineral deposits, and their sulfur isotope compositions and trace element characteristics can constrain the fluid and metal sources and ore-forming processes (Rye and Ohmoto, 1974; Huston et al., 1995; Large et al., 2009; Scott et al., 2009; Wagner et al., 2010; Ulrich et al., 2011; Zheng et al., 2013; Chen et al., 2015). Compared to bulk-grain sulfide analysis, *in-situ* microbeam-based sulfide trace element and sulfur isotope analyses can minimize inter/intra-grain contamination (especially where replacement textures are common) and enable the determination of intra-grain sulfur isotope and trace element variations (Ulrich et al., 2011; Chen et al., 2015).

Originally defined as a deposit class following the discovery of the

* Corresponding authors at: Key Laboratory of Mineralogy and Metallogeny, Guangzhou Institute of Geochemistry, Chinese Academy of Sciences, Guangzhou 510640, China (H. Chen).
E-mail address: huayongchen@gig.ac.cn (H. Chen).

https://doi.org/10.1016/j.oregeorev.2018.06.010
Received 10 February 2018; Received in revised form 11 June 2018; Accepted 12 June 2018
Available online 18 June 2018
0169-1368/ © 2018 Elsevier B.V. All rights reserved.

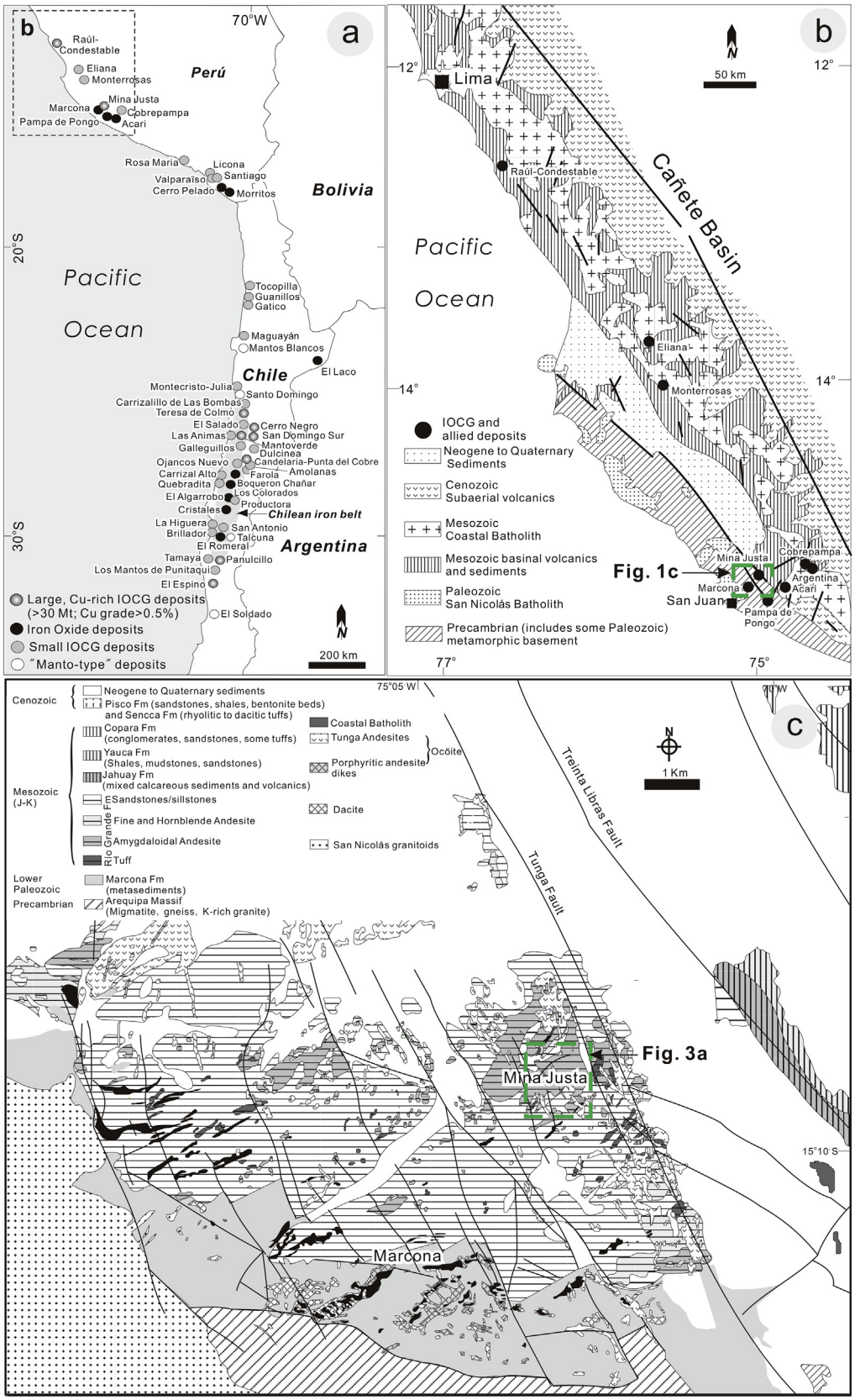

Fig. 1. Location of the Mina Justa IOCG deposit (modified after Chen et al., 2010).

giant Olympic Dam deposit (Australia), iron oxide copper-gold (IOCG) deposits have attracted much controversy regarding their ore genesis and deposit modeling (Hitzman et al., 1992; Williams et al., 2005; Groves et al., 2010; Sillitoe, 2003; Barton, 2013). Major arguments lie in the nature and source of the ore fluids of the Cu-Au mineralization stage, and their relationships with the (commonly earlier) Fe-oxide hydrothermal mineralization stage (Baker et al., 2001; Marschik and Fontbote, 2001; Sillitoe, 2003; Oliver et al., 2004; Pollard, 2006; Benavides et al., 2007; Chen et al., 2011). Particularly, whether external fluid was involved in the hydrothermal system, and (if present) contributed any Cu to the mineral system (Sillitoe, 2003; Benavides et al., 2007; Chen, 2013; Li and Zhou, 2018).

Many important IOCG deposits worldwide are hosted in Precambrian rocks (Williams et al., 2005), and their original hydrothermal characteristics are commonly variably masked by post-mineralization deformation and alteration. Therefore, young, undeformed and unmetamorphosed IOCG systems represent good research targets to resolve these metallogenic problems. Located in the South American Coastal Cordillera, the Mesozoic Central Andean IOCG province (Fig. 1a) is one of the world's youngest and best developed continental arc-related IOCG belts (Sillitoe, 2003). Different ore fluid origins have been proposed for the Central Andean IOCG province, including magmatic-hydrothermal (Marschik and Fontbote, 2001; Sillitoe, 2003 and references therein), non-magmatic (e.g., modified seawater) (Candelaria and Mantoverde, northern Chile; Ullrich et al., 2001; Benavides et al., 2007), and metamorphic brine (southern Perú; Vidal et al., 1990). Located in the Central Andes and hosted by the Jurassic upper Río Grande Formation (Fig. 1b, c), the Cretaceous Mina Justa Cu (Ag-Au) deposit has been assigned to the IOCG clan (Chen et al., 2010, 2011). The deposit hosts economic Cu mineralization, has a high Fe-oxide content, exhibits widespread sodic, calcic and potassic alterations, and is interpreted to have formed in an extensional continental arc setting. Seven stages of hydrothermal alteration and mineralization were recognized at Mina Justa: Stage I albite-actinolite alteration is followed by Stage II K-feldspar-magnetite alteration. Stage III alteration is composed mainly of prismatic actinolite, and Stage IV of specular hematite. No sulfide minerals are present in these early alteration stages. The most abundant sulfides at Mina Justa are pyrite in the Stage V magnetite-pyrite-K-feldspar alteration assemblage, and chalcopyrite, bornite and chalcocite in the Cu Stage VI mineralization assemblage. Stage V pyrite was pervasively replaced by Stage VI chalcopyrite veins (Chen et al., 2011), which raises the question of possible geochemical/isotopic inheritance in the chalcopyrite (Chen et al., 2011), which affects the determination of the sulfur source.

To better constrain the sulfide origin and genesis, to elucidate the ore fluid evolution in the different paragenetic stages, and to identify any possible sulfur and/or metal contribution from external fluids, we present new *in-situ* SIMS (secondary ion mass spectrometry) sulfur isotope and LA-ICP-MS (laser ablation inductively coupled plasma mass spectrometry) trace element data on the major sulfide minerals from Mina Justa.

2. Regional and deposit geology

The IOCG belt in southern Perú is underlain by the Paleoproterozoic to Mesoproterozoic Arequipa Massif Formation high-grade metamorphic rocks, including migmatite, gneiss, schist and meta-granite (Wasteneys et al., 1995; Loewy et al., 2004). Overlying this formation are the Neoproterozoic (San Juan Formation) and Paleozoic (Marcona Formation) sedimentary cover sequences (Caldas Vidal, 1978; Hawkes et al., 2002) (Fig. 2). The Marcona Formation (1500 m thick) hosts most of the magnetite orebodies at the Marcona Fe deposit (Fig. 2) and is overlain by thick Mesozoic meta-sedimentary/volcanic sequences, comprising (from bottom to top) the Río Grande, Jahuay, Yauca and Copara formations (Caldas Vidal, 1978). The Mina Justa Fe oxide Cu (Ag-Au) (abbrev. IOCG) deposit is hosted by the upper part of the Río Grande Formation (Fig. 2), which consists mainly of porphyritic andesite and andesitic volcaniclastic rocks with minor sandstone, conglomerate and mudstone (Caldas Vidal, 1978; Hawkes et al., 2002).

During the late Early to Late Cretaceous, the Peruvian coastal margin had likely undergone fast and oblique subduction, which led to widespread arc plutonism and the formation of five volcanosedimentary basins in the Western Peruvian Trough (WPT) (Polliand et al., 2005). The major two volcanosedimentary basins in the western WPT are named Huarmey (400 km long, 80 km wide) and Cañete (300 km long, 100 km wide), which appear separated but are in fact interconnected (Cobbing, 1978). The Mina Justa deposit lies on the margin of the Cañete Basin (Fig. 1b). Deposition of the Cañete Basin likely commenced in the Tithonian (152–145 Ma) and ceased in the Albian (113–100.5 Ma), representing a total lifespan of > 32 My (up to 51.5 My) (Cobbing, 1978). The Mina Justa deposit (Stage V: 104–101 Ma; Stage VI: 99–95 Ma; Chen et al., 2010) was formed during the late stage of the Cañete Basin development. The stratigraphic sequences of the Cañete Basin, from bottom to top, comprise shale (~1500 m thick), limestone (~1000 m thick) and marine volcaniclastic andesite (~4000 m thick) (Cobbing, 1978).

The widespread hydrothermal alteration in the Mina Justa area has masked much of the primary geochemical signatures of the Río Grande Formation andesitic wall rocks (Hawkes et al., 2002), but the same andesite unit (unaltered) located 40 km from Mina Justa is rich in Cu (average 400 ppm; Aguirre, 1988). NW-trending post-mineralization andesitic dikes are widespread and comprise about 35% of the total rock volume at Mina Justa (Fig. 3a; Chen et al., 2010). These plagioclase-phyric andesitic dikes have similar mineral contents to the Río Grande volcanic flows, but K-feldspar and sericite alterations are much weaker (Chen et al., 2010).

The Mina Justa deposit comprises the Main and Upper orebodies (Fig. 3b). These two lensoidal orebodies contain a magnetite-sulfide core surrounded by hydrothermal breccias that contain large (5–50 mm) angular host-rock clasts and magnetite-sulfide cement. The hydrothermal breccias are surrounded by extensive Cu-bearing stockwork ore. The orebodies are controlled by the NE-trending Mina Justa fault system (Chen et al., 2010), and displaced by the NW-trending Huaca faults and andesitic dikes. The main outcropping mineralized body contains supergene Cu oxides and albite-K-feldspar-actinolite alteration. Ore mineral zoning passes progressively downward from bornite-chalcocite-magnetite, through bornite-chalcopyrite-magnetite to chalcopyrite-pyrite-magnetite, whilst alteration zoning around the magnetite-sulfide orebody passes progressively outward from potassic, through calcic to sodic. Other supergene minerals identified at Mina Justa include chrysocolla, atacamite and hematite (Chen et al., 2010).

Our previous work had identified seven alteration/mineralization stages at Mina Justa (Fig. 4; Chen et al., 2010 and this study):

Stage I (sodic metasomatism) led to widespread albite replacement of plagioclase in the andesitic lavas and volcaniclastic host rocks. Stage II (K-Fe metasomatism) is mainly represented by K-feldspar and magnetite but without sulfide. Stage III (Ca metasomatism) lead to formation of massive aggregates of diopside, actinolite and minor magnetite. Stage IV minerals are dominated by specular hematite and calcite, with the former being almost entirely replaced by Stage V magnetite (Fig. 5a). Stage V (magnetite-pyrite) and Stage VI Cu sulfide mineralization contribute to the massive, lensoid and brecciated orebodies of the Mina Justa deposit.

Stage V magnetite occurs as granular (Fig. 5b–d) or tabular (Fig. 5c) aggregates, or as veins in some places (Fig. 5b). Stage V pyrite mainly occurs as aggregates (Fig. 5d) or veins (Fig. 5b), and in rare occasions some pyrite occurs in a frame of "mushketovite" (Fig. 5c). Magnetite and pyrite grains are subhedral to euhedral and 0.5 to 10 mm in diameter, with pyrite grains > 1 cm locally. Pyrite was always formed in the presence of magnetite, and the straight boundary between them indicates that the two minerals were formed together (Fig. 5b–d).

Major Stage VI metallic minerals include Cu sulfides (e.g.,

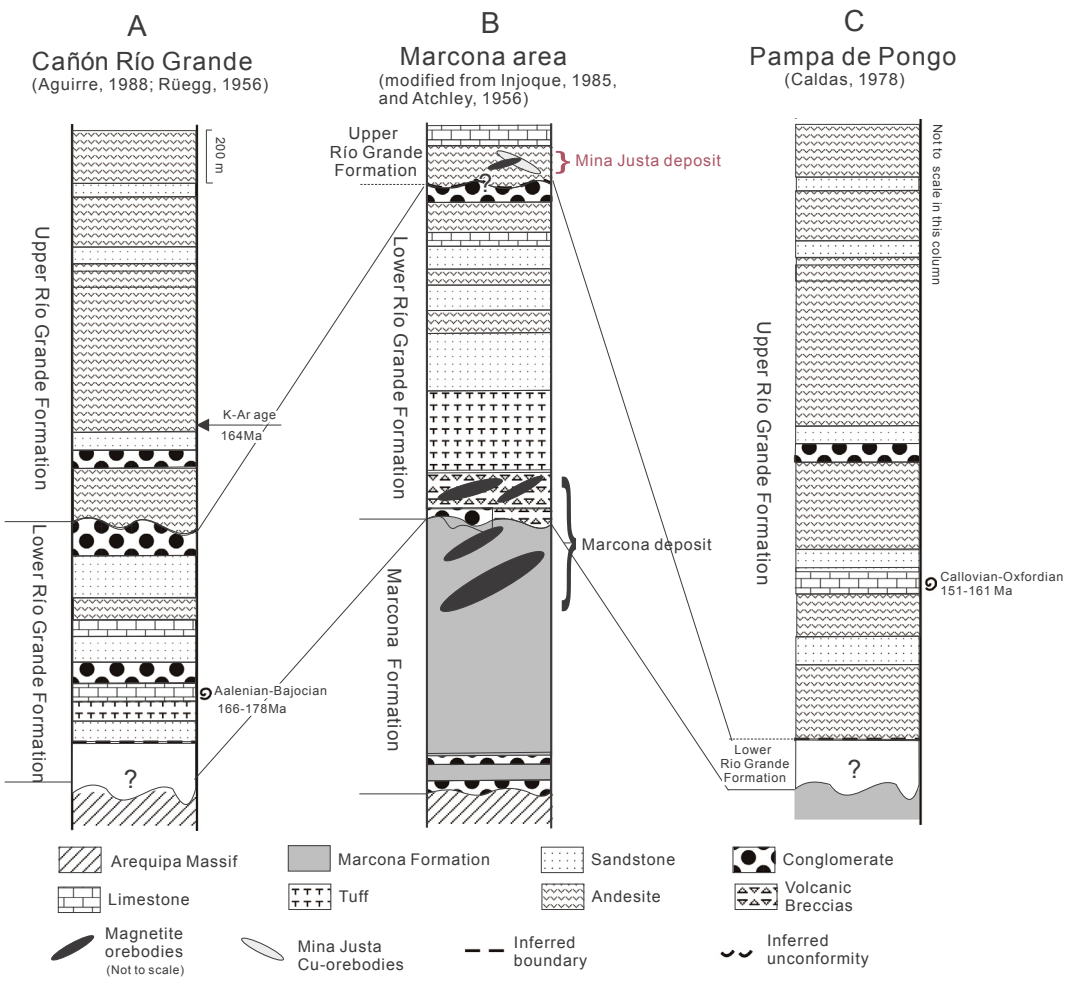

Fig. 2. Stratigraphic column of the Río Grand Formation in the Cañón Río Grande, Marcona, and Pampa de Pongo areas (modified after Chen et al., 2010).

chalcopyrite, bornite and chalcocite) (Fig. 5e, f), sphalerite and galena. Copper-bearing sulfides zone down-depth from chalcocite, through bornite to chalcopyrite (Fig. 3b). These sulfides usually form veins crosscutting earlier hydrothermal assemblages. In most cases, chalcopyrite occurs either as veins cutting Stage V pyrite or partially replaced it (Fig. 5c, f). Coexistence of chalcopyrite and bornite was locally observed, with local replacement of chalcopyrite by bornite (Fig. 5e). Chalcocite and bornite typically form patches with complex vermicular intergrowths (Fig. 14O in Chen et al., 2010).

Stage VII hematite locally developed in the upper parts of the orebodies. Specular hematite veins cut Stage III actinolite and Stage V magnetite, and Stage VII hematite replacing Stage V magnetite and Stage VI Cu mineralization is also present.

3. Sampling and analytical techniques

Samples were collected mainly from the chalcopyrite + pyrite (+magnetite) and bornite + chalcopyrite (+magnetite) mineralization zones (Appendix).

3.1. In-situ SIMS sulfur isotope analysis

The SIMS analysis was conducted at the Guangzhou Institute of Geochemistry, Chinese Academy of Sciences (GIGCAS) using a Cameca IMS1280-HR. A total of 231 spots on 15 sulfide samples (13 with both Stage V pyrite and Stage VI chalcopyrite, one with only pyrite, and one with only chalcopyrite) were analyzed. Analytical parameters are as follows:

Selected sulfide samples were mounted onto 25 mm diameter epoxy discs and polished. A primary $^{133}Cs^{+}$ ion beam (~2.0 nA current and 20 keV total impact energy) was focused at the sample surface with a spot diameter of 15 μm. A pre-sputtering period of 20 s was applied to remove the Au coating, and a normal-incidence electron gun was used for charge compensation. The mass resolving power was set at ~5000 to avoid isobaric interferences. An NMR field sensor was applied to stabilize the magnetic field. The isotopes of ^{32}S, ^{33}S and ^{34}S were measured simultaneously by the multi-collection system and the total analysis time for one spot was about 4 min. The primary standards used are PPP-1 (Gilbert et al., 2014) for pyrite and CPY-1 (in-house standard) for chalcopyrite (Molnár et al., 2016). The in-house standards Py-1 (Maier et al., 2016; Molnár et al., 2016) and CPY-2 were used as the secondary pyrite and chalcopyrite standards, respectively. The average $\delta^{34}S$ value we obtained on the standard Py-1 (−0.5 ± 0.3‰ (2σ); n = 21) is consistent with the recommended value (−0.6 ± 0.6‰ (2σ); Maier et al., 2016; Molnár et al., 2016). The secondary chalcopyrite standard CPY-2 was analyzed by two labs using a gas mass spectrometer, and our $\delta^{34}S$ result (average: −1.1 ± 1.2‰ (2σ); n = 18) is also consistent with the recommended value (−0.7 ± 1.0‰ (2σ).

Measured ratios of $^{34}S/^{32}S$ were normalized to the Vienna Canyon Diablo Troilite (V-CDT) value ($^{34}S/^{32}S$ = 1/22.6436, Ding et al. 2001), according to the following equations and taken as "raw" δ-value ($\delta^{34}S_{raw}$).

$$\delta^{34}S_{raw} = [(^{34}S/^{32}S)/(^{34}S/^{32}S)_{V\text{-}CDT} - 1] \times 1000$$

The Instrumental mass fractionation (IMF) is calculated from the

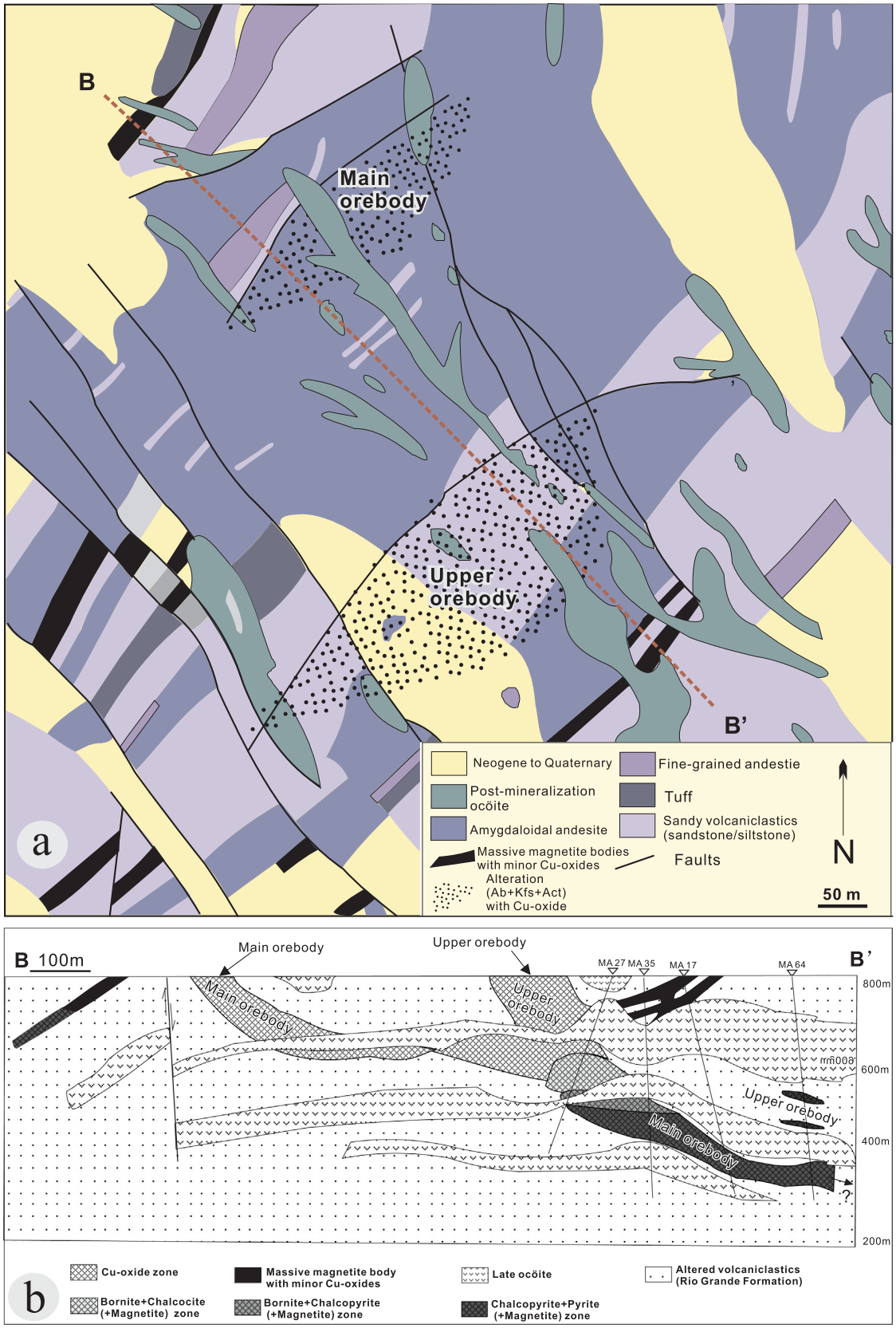

Fig. 3. (a) Geologic map of the Mina Justa IOCG deposit; (b) Cross section of B-B' in Fig. 3a.

known and the measured "raw" δ-value of standard samples:

$$IMF = \delta^{34}S_{standard\text{-}known} - \delta^{34}S_{standard\text{-}raw}$$

And the corrected $\delta^{34}S$ values of unknown samples is calculated as follows:

$$\delta^{34}S_{unknown\text{-}true} = \delta^{34}S_{unknown\text{-}raw} + IMF$$

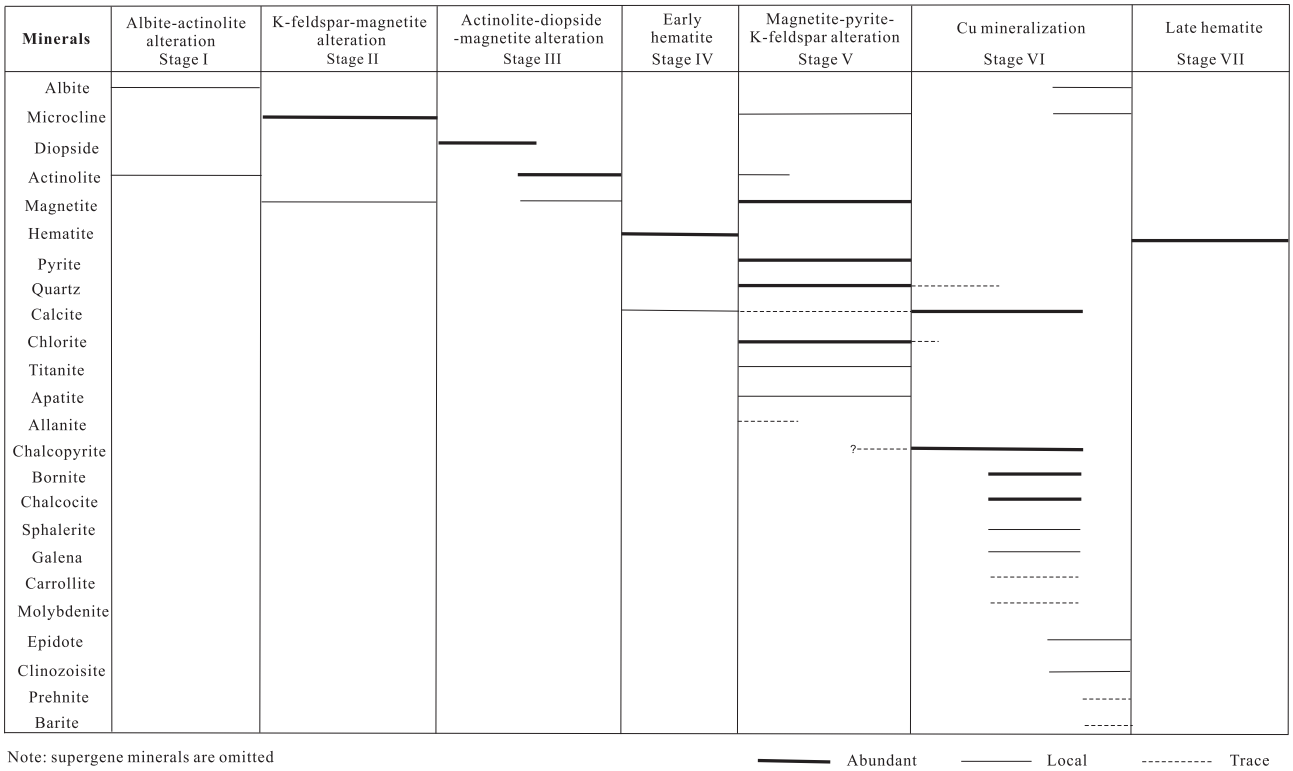

Fig. 4. Alteration and mineralization paragenesis at the Mina Justa IOCG deposit (modified after Chen et al., 2010).

The precision of the S-isotope analyses in this study, reported at the level of two standard errors (2σ), is better than 0.3‰.

3.2. In-situ LA-ICP-MS trace element analysis and WDS mapping

A total of 53 spots of five Stage V pyrite and Stage VI chalcopyrite samples (2 with both Stage V pyrite and Stage VI chalcopyrite, 2 with only pyrite, and 1 with only chalcopyrite) were analyzed by LA-ICP-MS. Before the LA-ICP-MS analysis, detailed petrographic and electron probe micro-analysis (EPMA) were undertaken to reveal any morphological and/or isotopic heterogeneity within individual sulfide grains. Element-distribution maps were acquired using a JEOL JXA-8230 EPMA instrument at the Key Laboratory of Mineralogy and Metallogeny, GIGCAS. The operating conditions include an accelerating voltage of 20 kV, probe current of 50nA and beam size of 4 μm. Elements and X-ray lines used for the analyses are Fe (Kα), As (Lα), Ni (Kα) and Co (Kα). The step size was 4 μm and the dwell time was set to be 100 ms for each point. The LA-ICP-MS analysis was conducted at CODES (ARC Centre of Excellence in Ore Deposits, University of Tasmania, Australia) using a New Wave 213-nm solid-state laser microprobe coupled with an Agilent 7500 Quadrupole ICP-MS. Detailed analysis parameters were as described by Large et al. (2007, 2009) and are summarized as follows. Target areas were ablated with a 47 μm diameter spot size. The laser repetition rate was 5 Hz, and the beam energy was maintained at about 7.2 J/cm^2. Data were collected in the time-resolved mode. The total analysis time for one spot was 90 s, which comprises 30 s measurement of background with laser off and 60 s analysis of sample with laser on. A total of 37 elements were analyzed.

All analyses were quantified against the STDGL2b2 standard (Danyushevsky et al., 2011), following the procedure of Longerich et al. (1996), and Fe was used as the internal standard. The STDGL2b2 standard was analyzed with a 100 μm beam at 10 Hz twice every 1.5 h to monitor the instrument drift. All results were linear drift-corrected. Mass-spectrometer drift was < 5 percent between each standard measurement.

4. Results

4.1. In-situ SIMS sulfur isotopes

The δ^{34}S values of Stage V pyrite ranges from −1.0 to +7‰ and show a possibly bimodal distribution (Fig. 6a). Many pyrite samples have homogeneous sulfur isotope compositions, but a few samples show clear microscale variations, e.g., the δ^{34}S values of sample DMA89-359.3 change sharply from +0.8‰ to +4.9‰ in a < 2 mm distance, showing distinct isotopic zoning (Fig. 7a), whilst those of sample DMA14-394.7 increase gradually from the core (+3.9‰) to rim (+6.0‰) (Fig. 7b).

The δ^{34}S distribution patterns of Stage VI chalcopyrite mimic those of Stage V pyrite, but with a narrower range (−0.6‰ to +4.6‰; Fig. 6b). Similar with their pyrite counterparts, the δ^{34}S values of Stage VI chalcopyrite are possibly slightly bimodal, mainly clustering between 0 and +4.0‰.

The Stage VI chalcopyrite with no apparent replacement relationship with Stage V pyrite (Fig. 7c) (and generally coexisting with bornite) shows no obvious δ^{34}S variation pattern (+0.9‰ to +1.2‰) (Fig. 7c). δ^{34}S values of the Stage VI chalcopyrite that replaced high-δ^{34}S Stage V pyrite (pyrite remnants: +3.3 to +4.4‰) are also high (+2.5 to +2.6‰; Fig. 7d), and the opposite is also true for the chalcopyrite (+0.6 to +0.9‰) that replaced low-δ^{34}S pyrite (pyrite remnants: +1.2 to +1.5‰; Fig. 7e).

4.2. LA-ICP-MS sulfide geochemistry

The most abundant trace elements in Stage V pyrite are Co (574 to 14823 ppm, average 5241 ppm), Ni (50 to 3327 ppm, average 1172 ppm), As (90 to 1189 ppm, average 255 ppm) and Se (14 to 94 ppm, average 44 ppm; Table 1). For the isotopically heterogeneous pyrite, the degree of δ^{34}S variation is accompanied by similar degree of

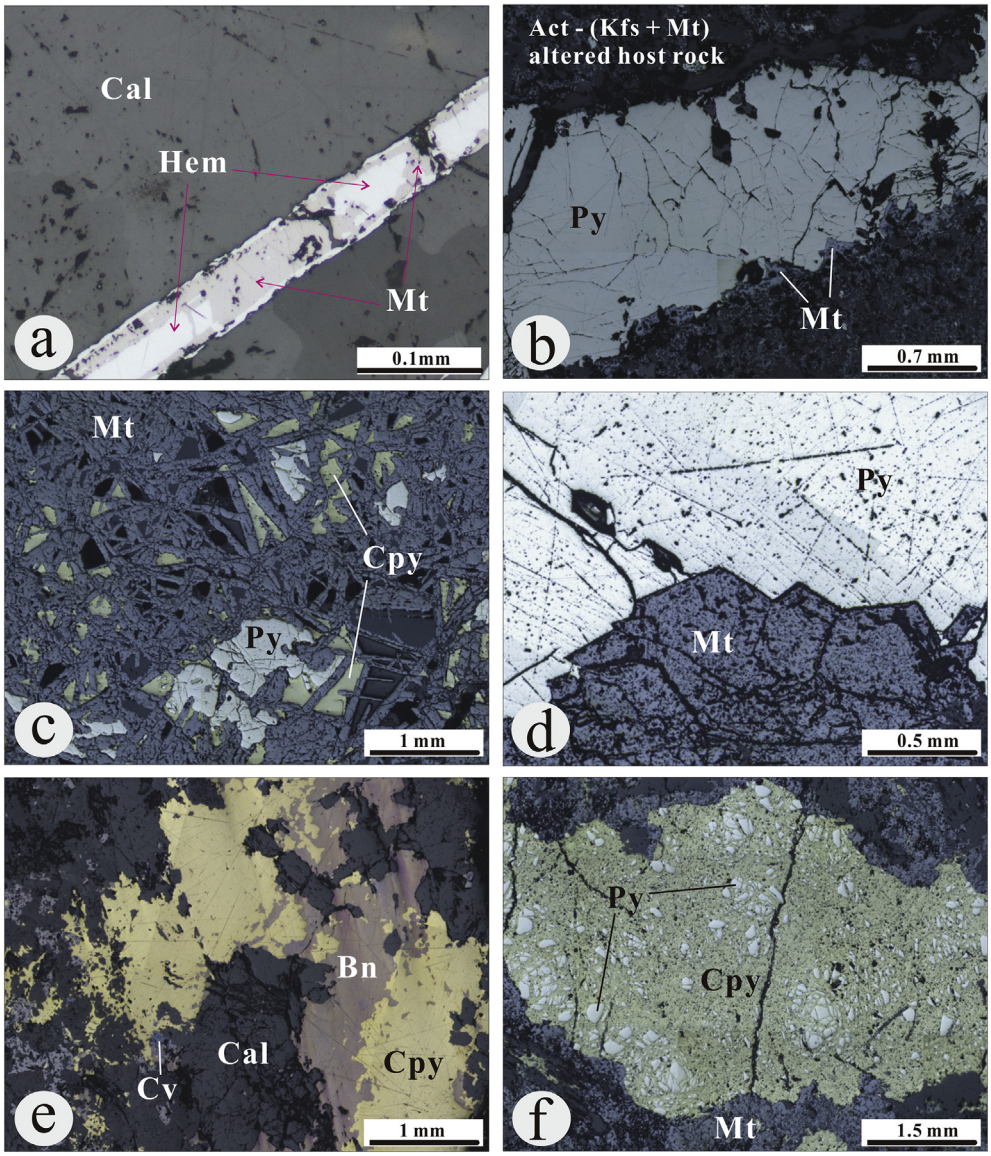

Fig. 5. Photographs and microphotographs of the Mina Justa IOCG ores: (a) Specular hematite replaced by Stage V magnetite (DMA35-507.9). (b) Stage V magnetite and pyrite vein crosscutting altered host rocks (DMA27-366.9). (c) Stage V tabular magnetite and associated pyrite. Pyrite partly replaced by Stage VI chalcopyrite (DMA35-507.9). (d) Stage V magnetite and pyrite (DMA45-272.6). (e) Stage VI chalcopyrite-bornite-calcite assemblage. (f) Stage V pyrite replaced by Stage VI magnetite (DMA89-322.1). Abbreviations: Mt: magnetite. Py: pyrite. Cpy: chalcopyrite. Cal: calcite. Act: actinolite. Kfs: K-feldspar. Cv: covellite. Bn: bornite.

trace element (e.g., Co, Ni, As and Se) concentration variation (Figs. 7a, b and 8a, b). Moreover, high-$\delta^{34}S$ pyrite tends to be Co-As richer and Ni-Se poorer (leading to higher Co/Ni ratios) relative to low-$\delta^{34}S$ pyrite (Figs. 8–10). The Se/S ratios of pyrite (0.3×10^{-4} to 1.4×10^{-4}) tend to decrease with increasing $\delta^{34}S$ values: $\delta^{34}S$ values increase to ca. +1.5‰ when the Se/S ratios decrease from 1×10^{-4} to 0.4×10^{-4} (Fig. 10a).

Intra-grain trace element (Co, Ni, Zn, As, Ag, Sn, Te, Pb and Bi) distributions in chalcopyrite are relatively heterogeneous except for Se (Table 2). Cobalt concentrations range from 0.3 to 1899 ppm, with the highest concentration (sample DMA89-322.1) being associated with Co-Ni-As-bearing inclusions (Fig. 11). Concentrations of Zn, Se, Ag, Sn, Pb and Bi range 1 to 235 ppm, 4 to 84 ppm, 1 to 68 ppm, 0 to 41 ppm, 0.1 to 47 ppm and 0 to 10 ppm, respectively (Table 2).

4.3. Sulfide WDS mapping

Wavelength dispersive spectrometry (WDS) analysis shows certain pyrite core-rim trace element zonation pattern: For instance, the core of pyrite DMA89-359.3 is Co-poor and Ni-rich, whereas the rim is Co-rich and Ni-poor (Fig. 12). Pyrite along the pyrite–chalcopyrite contact tends to be extremely Co- and As-rich (Fig. 12). In the samples DMA89-359.3 and DMA27-526.9, high $\delta^{34}S$ pyrite tends to be Co-rich and Ni-poor, consistent with the LA-ICP-MS results (Fig. 13).

5. Discussion

5.1. Ore-forming fluid source

Modeling is used here to constrain the source of sulfur and fluids for Stage V (Fig. 6c, d). The temperatures for modeling, obtained from oxygen isotope geothermometry of two mineral pairs (magnetite-quartz and magnetite-apatite), were set at 570 °C (540 °C to 600 °C, Chen et al., 2011). The fractionation between SO_4^{2-} and H_2S and pyrite-H_2S pairs are taken from Eldridge et al. (2016) and Ohmoto and Goldhaber (1997) respectively. Most of the $\delta^{34}S$ values of Stage V pyrite cluster between 0.5‰ and +2‰, corresponding to the fluid H_2S $\delta^{34}S$ values of −0.1‰ to +1.4‰ (the area between two solid black lines in Fig. 6c).

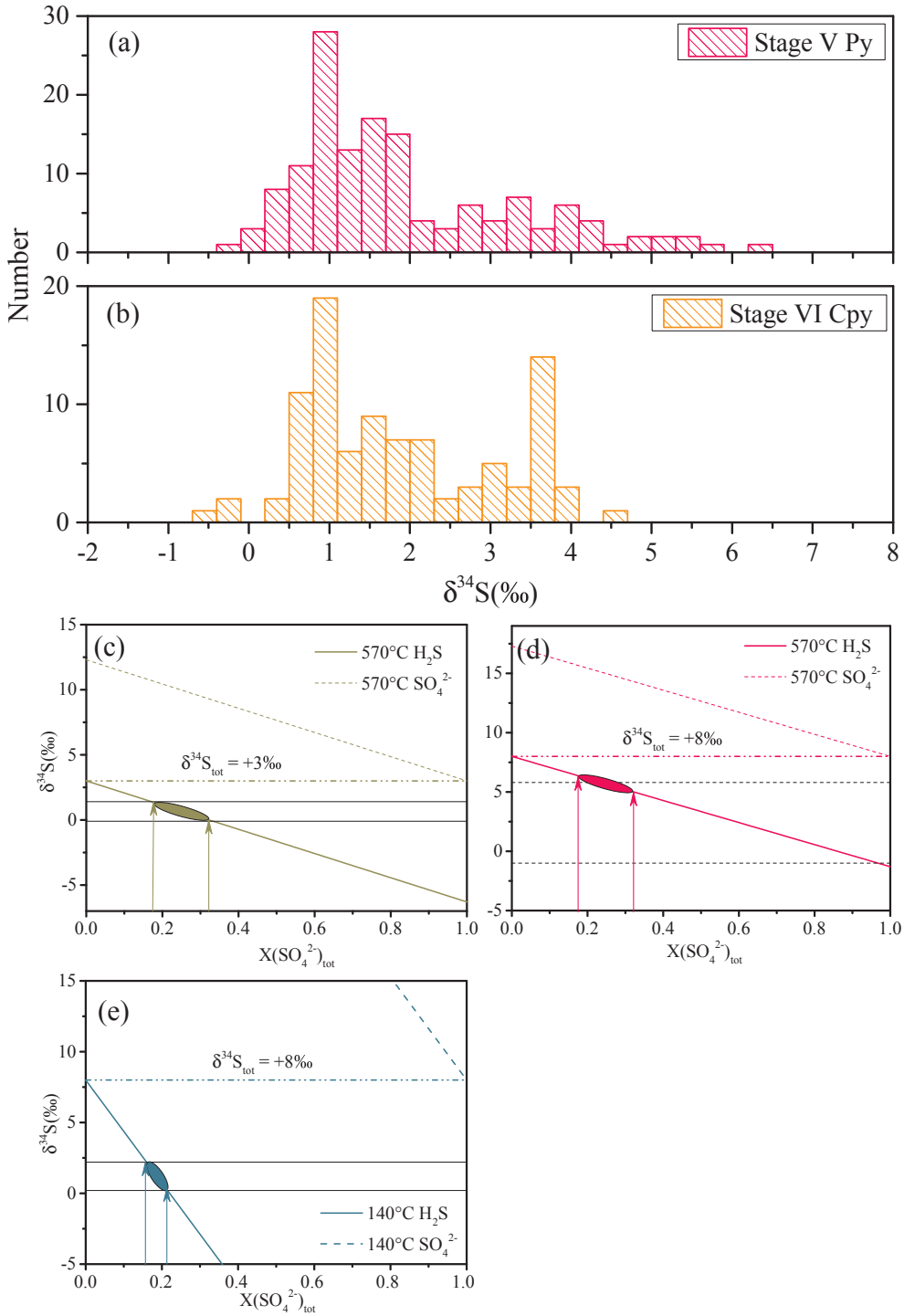

Fig. 6. (a): $\delta^{34}S$ histogram of the Stage V pyrite. (b): $\delta^{34}S$ histogram of the Stage VI chalcopyrite. (c) Modeling of the majority $\delta^{34}S$ value of the Stage V fluids. (d) Modeling of the heavy end of $\delta^{34}S$ value of the Stage V fluids. (e) Modeling of $\delta^{34}S$ value of the Stage VI fluids.

Given the presence of pyrite-magnetite assemblage, the fO_2 should be moderately reduced, meaning relatively low $[SO_4^{2-}/H_2S]$ ratios (Bastrakov et al., 2007; Schlegel et al., 2017). Therefore, these pyrite $\delta^{34}S$ values are consistent with $\Sigma\delta^{34}S_{fluid}$ of around +3‰ (Fig. 6c). However, the Stage V pyrite $\delta^{34}S$ values vary widely from −0.4‰ to +6.4‰, corresponding to the fluid H_2S $\delta^{34}S$ values of −1.0‰ to +5.8‰ (the area between two dashed black lines in Fig. 6d). We consider this wide $\delta^{34}S$ range (especially for the heavy end) of the fluid H_2S cannot be produced by a single magmatic fluid. At the pyrite-magnetite buffer, the fluids responsible for the heavy H_2S $\delta^{34}S$ values (+5.8‰) should have had $\delta^{34}S$ value of around +8‰ (Fig. 6d), which is clearly out of the magmatic range (Seal, 2006). Therefore, we suggest that the sulfur may have been mainly magmatic or from leaching of igneous rocks, and the sulfides with $\delta^{34}S$ values above +2.5‰ may have had contribution of sulfur from heavier sulfur isotope reservoirs (Ohmoto, 1972; Rye and Ohmoto, 1974; Seal, 2006). Here we set +2.5‰ as a boundary for the sake of discussion, mainly because our data are possibly slightly bimodal and +2.5‰ lies between these two groups (Fig. 6). Combined with the sharp drop of Se/S ratios and Co/Ni ratios higher than 1 at about +2.5‰ (Figs. 9 and 10), we believe these

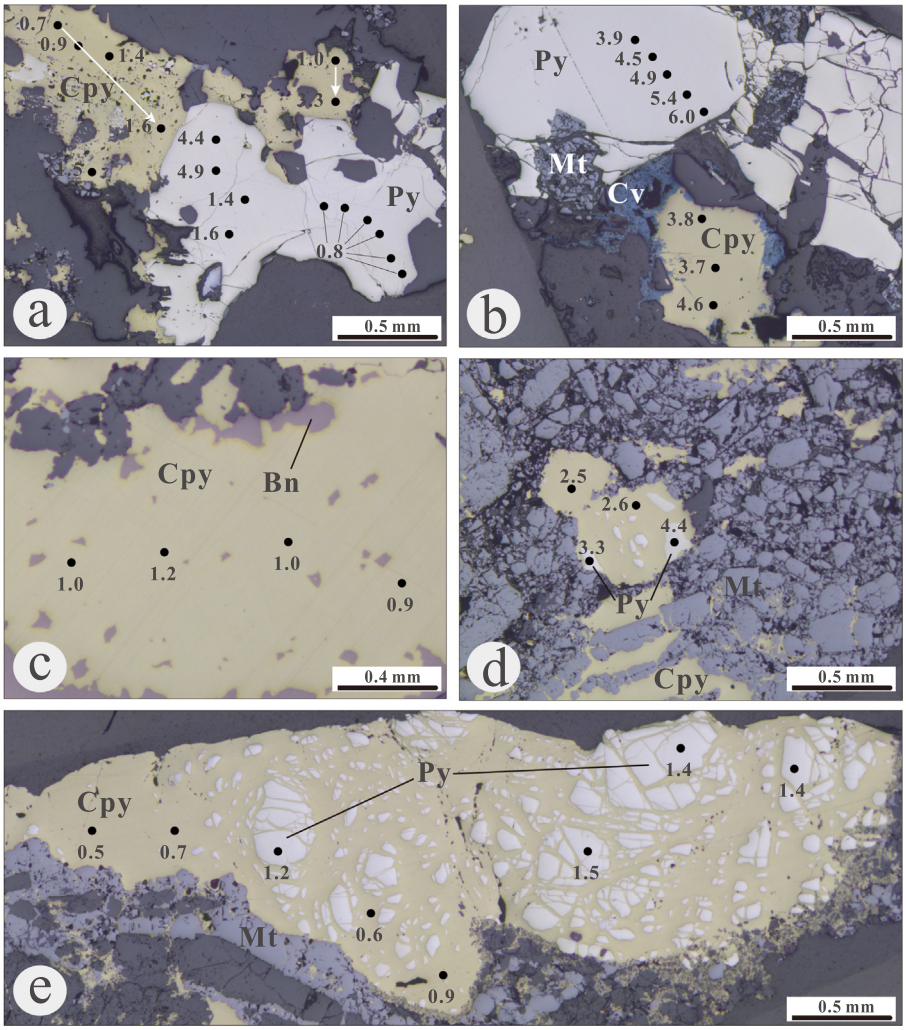

Fig. 7. Photomicrographs of the Mina Justa ore minerals (reflected light), showing the locations (black dots) and results (numbers next to black dots) of the *in-situ* sulfur isotope analysis. (a): Sample DMA89-359.3. Note the abrupt $\delta^{34}S$ increase from +0.8 to +4.9‰ in pyrite, and the gradual increase of chalcopyrite $\delta^{34}S$ values in the direction of the white arrows. (b): Sample DMA14-394.7. Note the increase of $\delta^{34}S$ values from core to rim in pyrite. (c): Sample DMA17-336.7. (d): Sample DMA27-509.5. (e): Sample DMA89-322.1. Py: pyrite, Cpy: chalcopyrite, Mt: magnetite, Bn: bornite, Cv: covellite.

two groups probably have different sulfur sources and/or involve different processes.

Since seawater (or basinal water) and magmatic fluids have stable but distinct Se/S ratios, they can provide information about the sulfur and selenium source (Huston et al., 1995; Rowins et al., 1997). Previous studies (Huston et al., 1995 and references therein; Seal, 2006) suggested that seawater (or basinal water) has average $\delta^{34}S$ value of around +21‰ and mass ΣSe/ΣS ratio of around $5-25\times10^{-8}$, whereas magmatic fluids have $\delta^{34}S$ value of around 0 ± 5‰ and mass ΣSe/ΣS ratio of around $1.2-5\times10^{-4}$. Our Mina Justa pyrite data show that the Se/S ratios also change with the $\delta^{34}S$ values (Fig. 8a), in which the low-$\delta^{34}S$ (~0‰) pyrite has high Se/S ratios (within the magmatic range), whereas the high-$\delta^{34}S$ (> +2.5‰) pyrite has low Se/S ratios (in the basinal-/seawater-derived water range; Fig. 8a). The sharp but continuous decrease of Se/S ratio at $\delta^{34}S$ = +1.5‰ (Fig. 10a) is consistent with the presence of two fluids, either mixing or sequentially involved within the IOCG ore-forming system.

As for the observed Se/S and sulfur isotope pattern (Figs. 7a, b and 10), possible explanations include the assimilation of sedimentary wall rocks into the magma and/or through Rayleigh fractionation. However, we consider neither process was likely, because (a) the deep-seated *syn*-mineralization dioritic stocks at Mina Justa (Chen et al., 2010) are not in direct contact with the sedimentary rocks in the area (Chen et al., 2010), (b) only minor sedimentary units occur with the submarine andesitic rocks, and (c) sedimentary wall rock assimilation would have been most extensive in early Stage V (due to its high temperature) and changed the sulfur isotope and trace element compositions of the early-formed pyrite, which is not observed in our study. All the lines above suggest that sedimentary wall rock assimilation was unlikely. Even though Rayleigh fractionation can partially account for the observed strongly-skewed distribution pattern, it is inconsistent with (assuming a closed system): (1) the $\delta^{34}S$ increase from the core to rim is coupled with a Co increase and Ni decrease (Figs. 8 and 12), yet Co and Ni (both compatible elements in pyrite; Loftus-Hills and Solomon, 1967; Price, 1972) contents in the fluids should be both decreasing gradually with decreasing temperature; (2) at > 350 °C, sulfur would partition preferentially into pyrite (relative to Se), leading to a ΣSe/ΣS increase in the fluids and thus a Se/S increase in the subsequent pyrite generation (Fitzpatrick, 2008). Similarly, ^{34}S is preferentially partitioned into pyrite (relative to the fluids), leading to a $\delta^{34}S$ decrease in the subsequent pyrite generation that is not observed either in our samples (Figs. 10 and 12). Therefore, we consider that the weak bimodal $\delta^{34}S$ distribution, the Co and Ni concentration variation and the Se/S pattern are more likely led by external fluid incursion. The Mina Jusa deposit was formed on the margin of the Cañete Basin, and the well-developed regional fault system that cut the Río Grande Formation could have

Table 1
Trace element concentrations (ppm) of Stage V pyrite at Mina Justa.

$\delta^{34}S$	Sample	Co	Ni	As	Se
−0.4	DMA27-526-Py1	7700	78	290	93
−0.4	DMA27-526-Py 2	7723	340	567	94
−0.3	DMA27-526-Py 3	8219	58	284	81
0.0	DMA27-526-Py 4	7427	50	281	91
1.5	DMA27-526-Py 5	13513	89	455	43
1.6	DMA27-526-Py 6	14648	72	397	36
1.6	DMA27-526-Py 7	12175	89	424	24
1.6	DMA27-526-Py 8	14823	71	353	36
1.7	DMA27-526-Py 9	13461	81	461	50
1.7	DMA27-526-Py 10	10434	155	457	48
1.1	DMA35-507-Py1	849	2797	453	52
1.2	DMA35-507-Py2	803	1431	531	37
1.3	DMA35-507-Py3	1202	2198	167	23
3.0	DMA35-507-Py4	5417	535	518	18
2.3	DMA35-507-Py5	2408	889	118	27
2.0	DMA35-507-Py6	262	3996	77	50
2.5	DMA35-507-Py7	7788	582	1189	28
2.8	DMA35-507-Py8	2807	1165	162	21
4.4	DMA89-359-Py1	11801	104	352	32
4.9	DMA89-359-Py2	12181	138	254	26
1.4	DMA89-359-Py3	2421	964	90	51
0.8	DMA89-359-Py4	897	2775	118	70
0.8	DMA89-359-Py5	494	2600	131	74
0.8	DMA89-359-Py6	691	3142	124	76
0.8	DMA89-359-Py7	739	3327	128	78
0.8	DMA89-359-Py8	587	3009	123	73
0.8	DMA89-359-Py9	589	2824	121	72
0.8	DMA89-359-Py10	574	2521	114	72
6.1	DMA14-394-Py1	5440	528	109	15
5.1	DMA14-394-Py2	4699	656	125	22
5.4	DMA14-394-Py3	4085	768	121	22
4.9	DMA14-394-Py4	3069	788	103	22
3.9	DMA14-394-Py5	3225	906	107	28
4.5	DMA14-394-Py6	3348	1001	102	27
5.0	DMA14-394-Py7	2827	1010	92	22
6.0	DMA14-394-Py8	3111	985	68	17
6.1	DMA14-394-Py9	3188	861	59	14
6.0	DMA14-394-Py10	3516	964	72	17

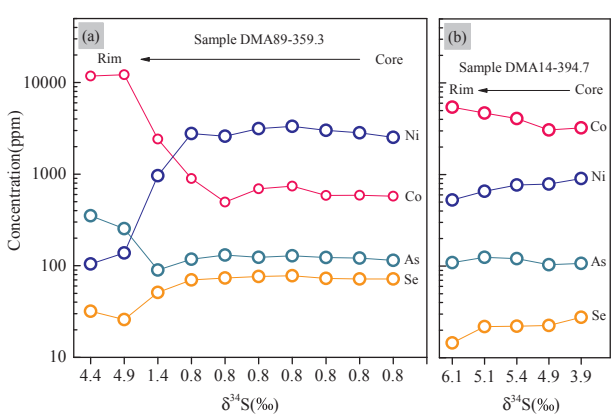

Fig. 8. Core-rim variation of element concentrations with $\delta^{34}S$ values of pyrite. Note the abrupt change of trace elements in (a) sample DMA89-359.3 and gradual change in (b) sample DMA14-394.7.

served as pathways for the external fluid incursion.

Sedimentary pyrite commonly contains low Co and Ni (both < 100 ppm) with Co/Ni < 1 (Loftus-Hills and Solomon, 1967; Price, 1972; Large et al., 2014), and the opposite is true for magmatic pyrite (Co and Ni both ~1000 s ppm with Co/Ni < 1) (Loftus-Hills and Solomon, 1967; Price, 1972; Bralia et al., 1979; Campbell and Ethier 1984). As for typical hydrothermal pyrite, the Co and Ni concentrations and Co/Ni ratios are highly varied, although the Co/Ni ratios are typically > 1 (up to 830) (Cook, 1996, Zhao and Zhou, 2011; Large et al., 2014; Li et al., 2014). At Mina Justa, the Co and Ni contents of the Stage V pyrite are commonly > 500 ppm, precluding a sedimentary origin. The wide pyrite Co/Ni range (0.2–202) (Fig. 9) that extends across those of the various reservoirs suggest the presence of diverse pyrite-forming fluid sources. Stage V pyrite with $\delta^{34}S$ values below +2.5‰ tends to have Co/Ni ratios below 1 (Fig. 9), which indicates a possible magmatic source. In contrast, the pyrite with higher $\delta^{34}S$ values (> +2.5‰) tends to have Co/Ni ratios above 3 (up to 113) (Fig. 9) and may indicate an external fluid contribution. The positive Co/Ni vs. $\delta^{34}S$ correlation indicates the incursion of a fluid with high Co/Ni and $\delta^{34}S$ values into the pyrite-forming fluid system (Fig. 9). The outlier of this trend (i.e., sample DMA27-526.9) contains low $\delta^{34}S$ values, high Co/Ni (Fig. 9) and varying Se/S ratios (Fig. 10a). The varying Se/S ratios (0.4×10^{-4} to 1.4×10^{-4}) suggest external fluid incursion, during which the Co-rich and Ni-Se-poor hydrothermal fluids may have substantially modified the trace element composition (e.g., Co, Ni and Se), resulting in the high Co/Ni and variable Se/S ratios obtained.

Laser ablation time-of-flight ICP-MS analyses of single fluid inclusions by Chen et al. (2011) shows that: the Stage VI fluid inclusions from calcite have lower Na (7.8 wt%), but higher Ca (2.5 wt%) and Fe (0.6 wt%) concentrations than those of Stage V. Stage VI fluid inclusions have eutectic and ice melting temperatures clustering around −45 °C to −50 °C and −20 °C to −25 °C, respectively (Chen et al., 2011). Therefore, Stage VI fluids are characterized by low-temperature, high-salinity and high-Ca content, which indicate basinal brine incursion during the Cu mineralization. Additionally, the oxygen and carbon isotopes of Stage VI fluid ($\delta^{18}O$, average +0.1‰; $\delta^{13}C$, average −8.3‰, calculated from the oxygen and carbon isotope compositions of Stage VI calcite; Chen et al., 2011) also shows basinal brine affinity (Longstaffe, 1987), further supporting our conclusion. Therefore, we propose that the Stage V pyrite core ($\delta^{34}S$ = ~0‰) was likely formed from a magmatic-derived source (Fig. 7a), whereas the rims of Stage V pyrite rim with higher $\delta^{34}S$ values (Fig. 7a, b) may have formed from external fluid (e.g., basinal brine) incursion (Chen et al., 2011).

Similar modeling was applied to constrain the source of Stage VI ore-forming fluids. The fractionation between SO_4^{2-} and H_2S and chalcopyrite-H_2S pairs are taken from Eldridge et al. (2016) and Li and Liu (2006) respectively. Previous fluid inclusion study (Chen et al., 2011) showed that most homogeneous temperature data cluster around 110 °C to 170 °C, and thus we used the median value (140 °C) for the modeling. The $\delta^{34}S$ values of Stage VI chalcopyrite with apparent replacement texture mimic those of the Stage V pyrite remnants, implying certain extent of isotopic inheritance. Consequently, $\delta^{34}S$ values of the Stage VI ore-forming fluids are best represented by those of the chalcopyrite without apparent replacement texture (i.e., +0.5‰ to +2.5‰, corresponding to the area between the two black solid lines in Fig. 6e). Although no magnetite was observed in Stage VI, the local coexistence of chalcopyrite-chalcocite-bornite leads us to speculate a moderately reducing condition for the Stage VI fluid system, with similar or lower [SO_4^{2-}/H_2S] ratios than that of Stage V. Under this condition, the total $\delta^{34}S$ value of the Stage VI ore fluids was constrained at about +8‰ (Fig. 6e), consistent with that (+8‰) of the high-$\delta^{34}S$ Stage V pyrite. This indicates that the ore-forming fluids in Stage VI and in late Stage V are basically the same, suggesting a continuous fluid evolution history from late Stage V to Stage VI at Mina Justa.

We suggest the sulfur of Stage VI (and late Stage V) were derived from more than one reservoir, and a binary mixing model involving leached-igneous and basinal-derived water is used to determine their respective sulfur contribution. According to the above discussion, we set the leached-igneous sulfur at +4‰ and basinal water at +21‰, yielding the contribution of leached-igneous and basinal water derived sulfur at about 76% and 24%, respectively. The Se/S ratio of leached-igneous derived fluids was set to be $1.4*10^{-4}$ (the highest value for Stage V pyrite), and basinal derived fluids was set to $15*10^{-8}$ (median value reported in Huston et al., 1995). Using the relative contribution of

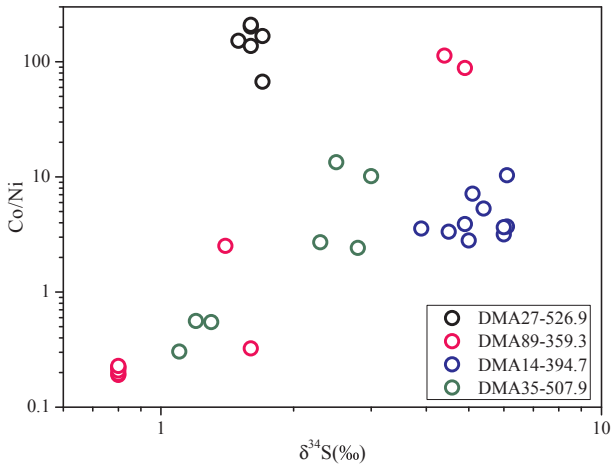

Fig. 9. Ni vs. Co diagram of Stage V pyrite. The few negative $\delta^{34}S$ values (n = 4) are omitted.

leached-igneous and basinal derived fluids discussed above (76% and 24% for leached-igneous and basinal derived fluids, respectively), and assuming the two reservoirs was well mixed, the chalcopyrite probably had Se/S ratios of around $1.06*10^{-4}$ (dashed orange line in Fig. 10b), well consistent with the average value ($1.04*10^{-4}$) obtained here (Fig. 10b). Consequently, we consider that the Stage VI ore fluids were derived from basinal brines leaching igneous rocks, which is very likely at isotopic and geochemical equilibrium after long reaction between the andesitic wall rocks and external fluids under low water/rock ratio.

5.2. Sources of metals

Given that the basinal-derived fluids commonly do not contain much Cu (< 1 ppb; Bruland, 1980), the possible Cu sources include leaching of andesite and/or directly from magmatic fluids. According to our model, we suggest that the basinal-derived fluids has likely attained equilibrium both isotopically (e.g., for sulfur) and geochemically (e.g., for Se). Thus, we speculate that Cu can also be leached from the andesite host rocks. Although magmatic fluids may represent a promising candidate for Cu source, and the absence of Cu-bearing mineral in Stage V was probably due to high temperature which inhibits Cu sulfide precipitation (Hezarkhani et al., 1999), the extra-long time gap between Stage V and Stage VI (about 5 My, Chen et al., 2010) indicates that continuous Cu sulfide precipitation with temperature decreasing was highly unlikely. Besides, fluid inclusions from Stage VI quartz were found to contain on average ~100 ppm Cu, but Cu was not detected in the inclusions from Stage V quartz (Chen et al., 2011). This indicates that, similar to sulfur, the copper of Stage VI mineralization may have derived from the leaching of Cu-rich andesitic wall rocks (average 400 ppm; Aguirre, 1988).

Previous studies indicated that the alteration of pyrite can release certain relatively mobile trace elements (e.g., Mo, Sb, Te, Au, Tl, Pb and Bi) from the mineral into the later-formed minerals (Large et al., 2007, 2009). Even though the less-mobile elements (e.g., Co, Ni and As, which form limited solid-solution series) tend to be retained in the altered pyrite (Large et al., 2009), they would also be released into the late-stage ore-forming fluids if the pyrite is (almost) totally replaced by chalcopyrite (Fig. 7e). We consider that the Co, Ni and As of the ore-forming fluids were mainly derived from Stage V pyrite, because: 1) Stage V pyrite are rich in Co, Ni and As (Table 1); 2) Co-Ni-As-rich mineral inclusions were only found in the chalcopyrite that (almost) totally replaced Stage V pyrite (Figs. 7e and 11); 3) Co-Ni-As-rich mineral inclusions are absent in the chalcopyrite that partially replaced Stage V pyrite (Fig. 7a). It is noteworthy that in samples DMA35-507.9 and DMA89-359.3, Zn concentration in the chalcopyrite (average: ~100 ppm) is much higher than that in pyrite (mostly < 10 ppm), and

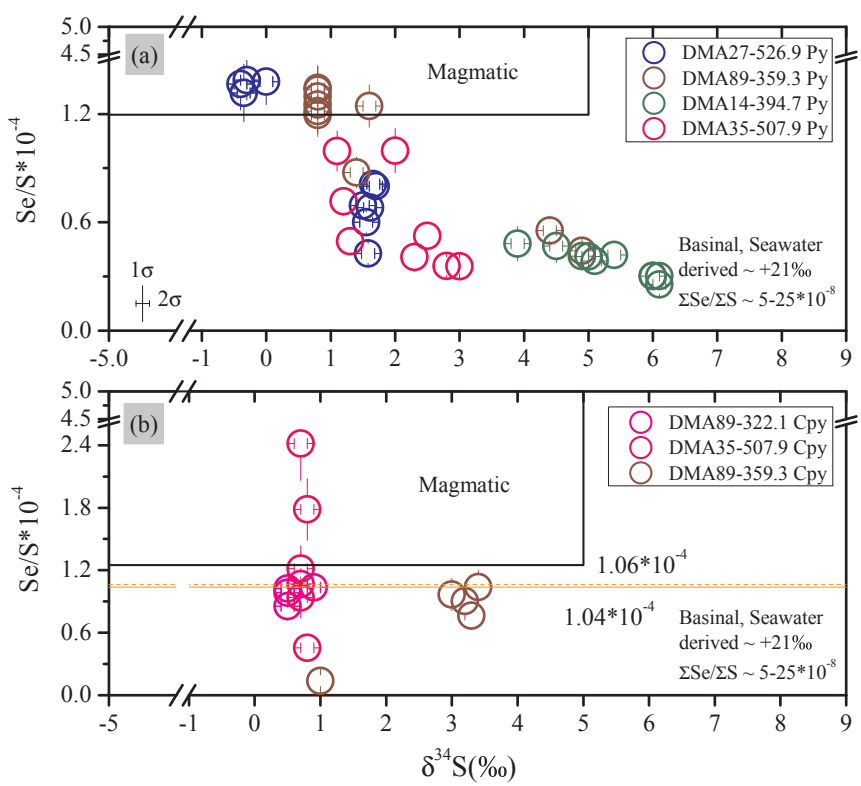

Fig. 10. Se/S × 10^{-4} vs. $\delta^{34}S$ diagram of (a) Stage V pyrite and (b) Stage VI chalcopyrite. The solid orange line in Fig. 10b is the average Se/S value ($1.04*10^{-4}$) of our results and the dashed orange line is the result ($0.95*10^{-4}$) derived our model.

Table 2
Trace element concentrations (ppm) of Stage VI chalcopyrite at Mina Justa.

$\delta^{34}S$	SampleName	Ti	Mn	Co	Ni	Zn	As	Se	Mo	Ag	Sn	Sb	Te	Au	Tl	Pb	Bi
0.7	DMA35-507-Cpy1	< 4.1160	< 0.9904	0.2847	0.0640	73	< 0.7592	33	0.0128	6	2.7736	0.3467	< 0.3660	< 0.0897	< 0.0316	1.8947	0.0563
0.7	DMA35-507-Cpy2	2.8208	< 1.0873	1.2997	0.0453	235	< 0.7301	84	< 0.1399	1	40.5341	0.0622	< 0.9422	< 0.0967	< 0.0327	0.2238	0.0138
0.7	DMA35-507-Cpy3	3.9132	< 0.9889	0.5466	0.0225	273	< 0.6907	42	0.0542	1	2.9715	< 0.1807	< 0.3866	0.0132	< 0.0455	0.1322	0.0114
0.8	DMA35-507-Cpy4	2.5308	2.0320	1.6743	< 0.1651	349	< 0.8758	62	< 0.0993	1	50.2677	0.1470	< 0.7793	0.0200	< 0.0408	0.5449	< 0.0372
0.8	DMA35-507-Cpy5	2.2720	< 1.2047	0.8251	0.0229	84	< 0.7094	16	< 0.1404	3	14.3049	< 0.1408	< 0.7884	< 0.0494	< 0.0563	0.1179	< 0.0170
3.4	DMA89-359-Cpy1	2.9621	1.4929	0.2488	0.0356	98	< 0.5728	36	< 0.0843	63	< 0.1478	0.1408	8.6582	< 0.0342	< 0.0403	34.5007	2.2721
3.0	DMA89-359-Cpy2	3.8633	1.2621	0.1601	< 0.3189	76	< 0.5934	34	0.0909	68	0.1789	0.2044	9.3361	< 0.0269	< 0.0123	47.3176	2.7998
3.2	DMA89-359-Cpy3	1.2274	3.6492	0.1851	0.0308	99	< 0.5419	31	< 0.0000	62	0.1401	0.2102	9.7393	< 0.0510	0.0075	29.3296	1.9562
3.3	DMA89-359-Cpy4	< 2.0352	0.9436	0.1171	< 0.2721	34	< 0.6725	27	0.0252	64	0.2031	0.1459	5.2914	0.0310	0.0251	17.9268	1.5916
1.0	DMA89-359-Cpy5	4.8922	19.678	0.1302	0.3784	35	< 0.4247	5	0.0448	54	0.1080	0.4784	< 0.5552	0.0778	< 0.0267	1.7983	0.8180
0.7	DMA89-322-Cpy1	2.7525	< 1.0265	168.8419	7.2877	2	5.6659	37	< 0.0839	38	< 0.1546	1.3287	< 0.5048	0.0810	< 0.0425	30.4076	10.4965
0.9	DMA89-322-Cpy2	3.6765	< 0.6734	1899.485	49.6817	1	33.8402	36	< 0.0000	27	< 0.1228	0.6738	< 0.4287	< 0.0244	0.06947	19.8766	6.7915
0.5	DMA89-322-Cpy3	< 5.3057	< 0.9602	30.40439	3.0524	1	60.5762	36	0.0369	49	0.1962	0.9145	< 1.0464	< 0.0520	< 0.0370	25.2844	7.5388
0.5	DMA89-322-Cpy4	4.7592	< 0.8941	12.85474	1.1529	1	28.0172	34	0.0238	31	0.2248	1.3993	< 0.5241	0.0498	< 0.0509	25.7630	7.7935
0.5	DMA89-322-Cpy5	< 3.4664	1.2993	6.54015	0.5830	2	10.7620	30	0.0118	28	< 0.1724	1.0008	< 0.6315	0.0399	< 0.0506	18.3827	5.8612

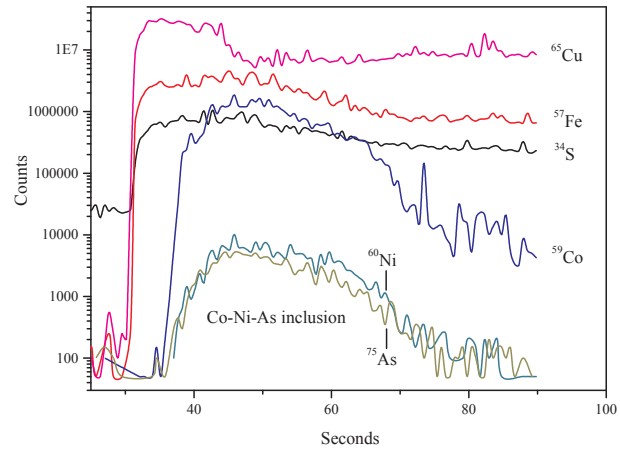

Fig. 11. LA-ICP-MS signal of DMA89-322.1 chalcopyrite.

(for sample DMA89-359.3) higher Ag and Pb concentrations are also found in the chalcopyrite (Tables 1 and 2). This suggests that the enrichments in Zn (and/or Ag and Pb) in the Stage VI chalcopyrite were derived from the ore-forming fluids rather than from Stage V pyrite (Table 2). Pyrite along the contacts with chalcopyrite tends to be extremely Co-As rich but Fe poor (Fig. 12), and this only occurs where chalcopyrite is present. This suggests that many trace elements (e.g., Co, As and/or Ni) in pyrite that were previously considered to be immobile (Large et al., 2009) may actually be mobilized by low temperature (~130 °C) hydrothermal alteration (Chen et al., 2011).

5.3. Evolution of the ore-forming fluids

The Pacific Plate subduction beneath the western margin of the South American Plate has likely led to arc crustal attenuation and the subsequent ascent of deep-sourced andesitic magmas (Sillitoe, 2003). Local extension of the converging plates resulted in many mid-Cretaceous volcano-sedimentary basins (Polliand et al., 2005), and the continued convergence eventually led to uplift, basin inversion, and formation of the ore-controlling fault system (Fig. 1c). During early Stage V, the pyrite-forming fluid system may have been of high temperature and predominantly magmatic, which formed the low-$\delta^{34}S$ pyrite with low Co/Ni and high Se/S ratios (Figs. 6, 9 and 10). During late Stage V, the well-developed fault system may have facilitated minor external fluid (possibly basinal brine) incursion into the pyrite-forming fluid system and resulted in the high-$\delta^{34}S$ pyrite with varying Co/Ni and Se/S ratios (Figs. 6, 7a, 9 and 10). With increasing external fluid input, $\delta^{34}S$ values of the Stage V pyrite gradually increased from +3.9‰ to +6.0‰ (Fig. 7b), and trace element concentrations also changed gradually (Co and As increased, and Ni and Se decreased; Fig. 8b).

At Mina Justa, the Cu mineralization temperature was relatively low (90 °C to 220 °C, mode of ~130 °C; Chen et al., 2011), and we propose that the heat may have come primarily from the residual heat of past magmatism or deep-seated plutons (Chen et al., 2010). The Cu ore-forming fluids may have derived from basinal brine (Chen et al., 2011), which may have resided and reacted with the andesitic wall rocks for about 2–5 My (Chen et al., 2010; 2011), and reached isotopic equilibrium with the andesite. During the reaction, the ore-forming fluids may have leached metals and sulfur from the Cu-rich (average 400 ppm; Aguirre, 1988) andesitic wall rocks (Figs. 6 and 7c). At about 99 to 95 Ma (Chen et al., 2010), Stage VI chalcopyrite may have replaced Stage V pyrite, thus inheriting part of the sulfur isotopic and trace element signatures (Figs. 6 and 7a, d, e; Tables 1 and 2).

6. Conclusion

Sulfur isotope and trace element features of the pyrite in Stage V

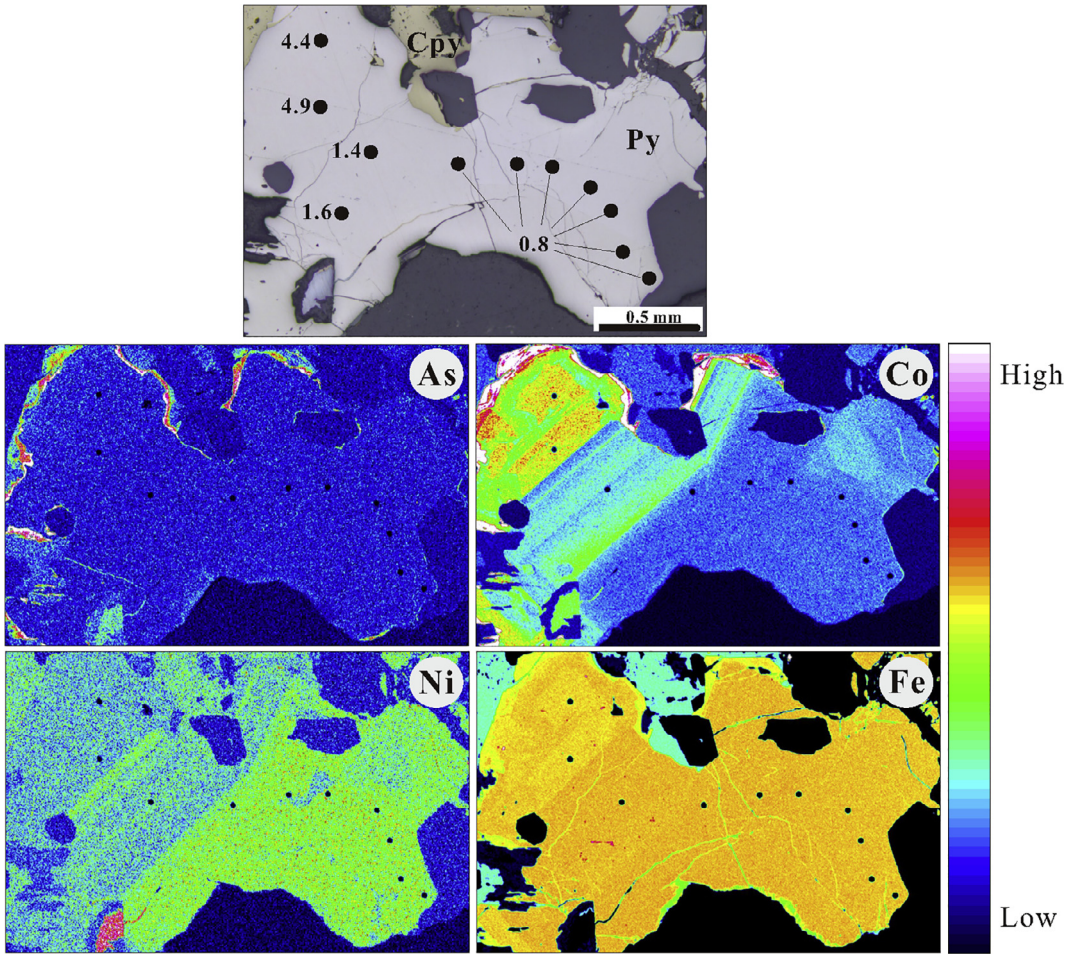

Fig. 12. WDS mapping of As, Co, Ni and Fe (DMA89-359.3).

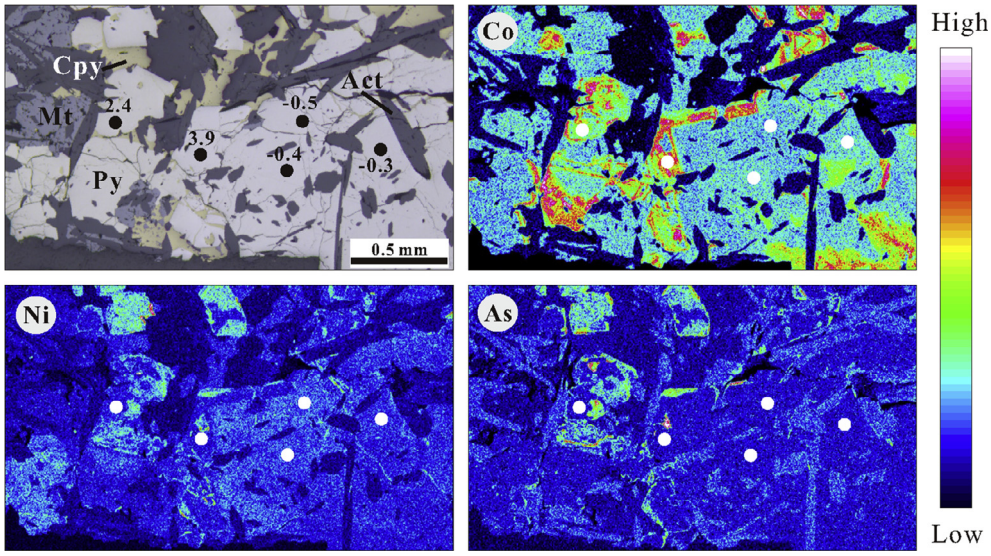

Fig. 13. WDS mapping of Co, Ni and As (DMA27-526.9).

(magnetite-pyrite) suggest external fluid incursion into the dominantly magmatic fluid system at Mina Justa. External fluids were likely responsible for the Stage VI Cu mineralization. Sulfur was likely sourced from the leaching of the Mesozoic andesitic wall rocks. The fluids had likely altered and assimilated Stage V pyrite, from which Stage VI chalcopyrite may have inherited the geochemical and sulfur isotope characteristics, although influence of magmatic fluid mixing cannot be excluded. Some trace elements (e.g., Zn, Ag and Pb) in the chalcopyrite may have come mainly from the Stage VI Cu ore-forming fluids, and other elements (e.g., Co, Ni, As, Se, Mo, Sb, Te, Au, Tl and Bi) may have come from the pyrite they replaced. Additionally, some trace elements (notably Co, As and/or Ni) that were previously considered to be

immobile in pyrite may actually be mobilized by low temperature hydrothermal alteration. This study leads us to reconsider the effect of non-magmatic fluid incursion during Cu mineralization in IOCG deposits, and suggests that some (precious) metals may be mobilized and enriched via the replacement of earlier sulfides by later ones.

Acknowledgements

This research was jointly supported by the Guangzhou Municipal Government (201607020029), the Chinese National Basic Research 973-Program (2014CB440802), National Natural Science Foundation of China (41572059), CAS-SAFEA International Partnership Program for Creative Research Team (20140491534) and the CAS 100 Talent Program (Y333081A07). We are grateful to two anonymous reviewers for their thorough reviews and insightful suggestions. We would like to thank Chao Wu for the LA-ICP-MS analysis and Chang-Ming Xing for the EPMA analysis.

Appendix A. Supplementary data

Supplementary data associated with this article can be found, in the online version, at https://doi.org/10.1016/j.oregeorev.2018.06.010.

References

Aguirre, L., 1988. Chemical mobility during low-grade metamorphism of a Jurassic lava flow: Río Grande Formation, Perú. J. South Am. Earth Sci. 1, 343–361.
Baker, T., Perkins, C., Blake, K.L., Williams, P.J., 2001. Radiogenic and stable isotope constraints on the genesis of the Eloise Cu-Au deposit, Cloncurry district, northwest Queensland. Econ. Geol. Bull. Soc. Econ. Geol. 96, 723–742.
Barton, M., 2013. Iron oxide (-Cu-Au-REE-P-Ag-U-Co) systems. Treatise on Geochemistry, second ed. Elsevier Inc.
Bastrakov, E.N., Skirrow, R.G., Davidson, G.J., 2007. Fluid evolution and origins of iron oxide Cu-Au prospects in the Olympic Dam district, Gawler craton, South Australia. Econ. Geol. 102, 1415–1440.
Benavides, J., Kyser, T.K., Clark, A.H., Oates, C.J., Zamora, R., Tarnovschi, R., Castillo, B., 2007. The Mantoverde iron oxide copper-gold district, III region, Chile: The role of regionally derived, nonmagmatic fluids in chalcopyrite mineralization. Econ. Geol. 102, 415–440.
Bralia, A., Sabatini, G., Troja, F., 1979. A revaluation of the Co/Ni ratio in pyrite as geochemical tool in ore genesis problems. Miner. Deposita 14, 353–374.
Bruland, K.W., 1980. Oceanographic distributions of cadmium, zinc, nickel, and copper in the North Pacific. Earth Planet. Sci. Lett. 47, 176–198. https://doi.org/10.1016/0012-821X(80)90035-7.
Caldas Vidal, J., 1978. Geología de los cuadrángulos de San Juan, Acarí y Yauca: hojas, (31-m, 31-n, 32-n). Instituto de Geología y Minería, Lima, Peru.
Campbell, F.A., Ethier, V.G., 1984. Nickel and cobalt in pyrrhotite and pyrite from the Faro and Sullivan orebodies. Can. Minera. 22, 503–506.
Chen, H., Kyser, T.K., Clark, A.H., 2011. Contrasting fluids and reservoirs in the contiguous Marcona and Mina Justa iron oxide–Cu (–Ag–Au) deposits, south-central Perú. Miner. Deposita 46, 677–706.
Chen, H.Y., Clark, A.H., Kyser, T.K., Ullrich, T.D., Baxter, R., Chen, Y.M., Moody, T.C., 2010. Evolution of the giant marcona-mina justa iron oxide-copper-gold district, south-central Peru. Econ. Geol. 105, 155–185.
Chen, H.Y., 2013. External sulphur in IOCG mineralization: implications on definition and classification of the IOCG clan. Ore Geol. Rev. 51, 74–78.
Chen, L., Li, X.H., Li, J.W., Hofstra, A.H., Liu, Y., Koenig, A.E., 2015. Extreme variation of sulfur isotopic compositions in pyrite from the Qiuling sediment-hosted gold deposit, West Qinling orogen, central China: an in situ SIMS study with implications for the source of sulfur. Miner. Deposita 50, 643–656.
Cobbing, E., 1978. The Andean geosyncline in Peru, and its distinction from Alpine geosynclines. J Geol Soc 135, 207–218.
Cook, N.J., 1996. Mineralogy of the sulphide deposits at Sulitjelma, northern Norway. Ore Geol. Rev. 11, 303–338.
Danyushevsky, L., Robinson, P., Gilbert, S., Norman, M., Large, R., McGoldrick, P., Shelley, M., 2011. Routine quantitative multi-element analysis of sulphide minerals by laser ablation ICP-MS: Standard development and consideration of matrix effects. Geochem-Explor Env A 11, 51–60.
Ding, T., Valkiers, S., Kipphardt, H., De Bievre, P., Taylor, P.D.P., Gonfiantini, R., Krouse, R., 2001. Calibrated sulfur isotope abundance ratios of three IAEA sulfur isotope reference materials and V-CDT with a reassessment of the atomic weight of sulfur. Geochim. Cosmochim. Acta 65, 2433–2437 Doi 10.1016/S0016-7037(01)00611-1.
Eldridge, D.L., Guo, W., Farquhar, J., 2016. Theoretical estimates of equilibrium sulfur isotope effects in aqueous sulfur systems: highlighting the role of isomers in the sulfite and sulfoxylate systems. Geochim. Cosmochim. Acta 195, 171–200.
Fitzpatrick, A.J. 2008. The measurement of the Se/S ratios in sulphide minerals and their application to ore deposit studies.
Gilbert, S.E., Danyushevsky, L.V., Rodemann, T., Shimizu, N., Gurenko, A., Meffre, S., Thomas, H., Large, R.R., Death, D., 2014. Optimisation of laser parameters for the analysis of sulphur isotopes in sulphide minerals by laser ablation ICP-MS. J Anal At Spectrom 29, 1042–1051.
Groves, D.I., Bierlein, F.P., Meinert, L.D., Hitzman, M.W., 2010. Iron oxide copper-gold (IOCG) deposits through earth history: implications for origin, lithospheric setting, and distinction from other epigenetic iron oxide deposits. Econ. Geol. 105, 641–654.
Hawkes, N., Clark, A., Moody, T., 2002. Marcona and Pampa de Pongo: giant Mesozoic Fe-(Cu, Au) deposits in the Peruvian coastal belt. Hydrothermal iron oxide copper-gold and related deposits: A global perspective: Adelaide, Porter Geoscience Consultancy Publishing 2:115–130.
Hezarkhani, A., Williams-Jones, A., Gammons, C., 1999. Factors controlling copper solubility and chalcopyrite deposition in the Sungun porphyry copper deposit. Iran. Miner Deposita 34, 770–783.
Hitzman, M.W., Oreskes, N., Einaudi, M.T., 1992. Geological characteristics and tectonic setting of proterozoic iron-oxide (Cu-U-Au-Ree) deposits. Precambr. Res. 58, 241–287.
Huston, D.L., Sie, S.H., Suter, G.F., Cooke, D.R., Both, R.A., 1995. Trace-elements in sulfide minerals from eastern australian volcanic-hosted massive sulfide deposits. 1. Proton microprobe analyses of pyrite, chalcopyrite, and sphalerite, and. 2. Selenium levels in pyrite – comparison with delta-S-34 values and implications for the source of sulfur in volcanogenic hydrothermal systems. Econ. Geol. Bull. Soc. Econ. Geol. 90, 1167–1196.
Large, R.R., Danyushevsky, L., Hollit, C., Maslennikov, V., Meffre, S., Gilbert, S., Bull, S., Scott, R., Emsbo, P., Thomas, H., Singh, B., Foster, J., 2009. Gold and trace element zonation in pyrite using a laser imaging technique: implications for the timing of gold in orogenic and carlin-style sediment-hosted deposits. Econ. Geol. 104, 635–668.
Large, R.R., Halpin, J.A., Danyushevsky, L.V., Maslennikov, V.V., Bull, S.W., Long, J.A., Gregory, D.D., Lounejeva, E., Lyons, T.W., Sack, P.J., McGoldrick, P.J., Calver, C.R., 2014. Trace element content of sedimentary pyrite as a new proxy for deep-time ocean–atmosphere evolution. Earth Planet. Sci. Lett. 389, 209–220. https://doi.org/10.1016/j.epsl.2013.12.020.
Large, R.R., Maslennikon, V.V., Robert, F., Danyushevsky, L.V., Chang, Z.S., 2007. Multistage sedimentary and metamorphic origin of pyrite and gold in the giant Sukhoi Log deposit, Lena gold province, Russia. Econ. Geol. 102, 1233–1267.
Li, N., Deng, J., Yang, L.Q., Goldfarb, R.J., Zhang, C., Marsh, E., Lei, S.B., Koenig, A., Lowers, H., 2014. Paragenesis and geochemistry of ore minerals in the epizonal gold deposits of the Yangshan gold belt, West Qinling, China. Miner. Deposita 49, 427–449.
Li, X.-C., Zhou, M.-F., 2018. The nature and origin of hydrothermal REE mineralization in the sin quyen deposit, Northwestern Vietnam. Econ. Geol. 113, 645–673.
Li, Y., Liu, J., 2006. Calculation of sulfur isotope fractionation in sulfides. Geochim. Cosmochim. Acta 70, 1789–1795.
Loewy, S.L., Connelly, J.N., Dalziel, I.W.D., 2004. An orphaned basement block: the Arequipa-Antofalla basement of the central Andean margin of South America. Geol. Soc. Am. Bull. 116, 171–187.
Loftus-Hills, G., Solomon, M., 1967. Cobalt, nickel and selenium in sulphides as indicators of ore genesis. Miner. Deposita 2, 228–242. https://doi.org/10.1007/BF00201918.
Longerich, H.P., Jackson, S.E., Gunther, D., 1996. Laser ablation inductively coupled plasma mass spectrometric transient signal data acquisition and analyte concentration calculation. J Anal. At. Spectrom. 11, 899–904.
Longstaffe, F., 1987. Stable isotope studies of diagenetic processes. In stable isotope geochemistry of low temperature processes. Short Course Handbook 13, 187–257.
Maier, W.D., Smithies, R.H., Spaggiari, C.V., Barnes, S.J., Kirkland, C.L., Yang, S., Lahaye, Y., Kiddie, O., MacRae, C., 2016. Petrogenesis and Ni-Cu sulphide potential of mafic-ultramafic rocks in the Mesoproterozoic Fraser Zone within the Albany-Fraser Orogen, Western Australia. Precambr. Res. 281, 27–46. https://doi.org/10.1016/j.precamres.2016.05.004.
Marschik, R., Fontbote, L., 2001. The Candelaria-Punta del Cobre iron oxide Cu-Au(-Zn-Ag) deposits, Chile. Econ. Geol. Bull. Soc. Econ. Geol. 96, 1799–1826.
Molnár, F., Mänttäri, I., O'Brien, H., Lahaye, Y., Pakkanen, L., Johanson, B., Käpyaho, A., Sorjonen-Ward, P., Whitehouse, M., Sakellaris, G., 2016. Boron, sulphur and copper isotope systematics in the orogenic gold deposits of the Archaean Hattu schist belt, eastern Finland. Ore Geol. Rev. 77, 133–162.
Ohmoto, H., 1972. Systematics of Sulfur and Carbon Isotopes in Hydrothermal Ore-Deposits. Econ. Geol. 67, 551–578.
Ohmoto, H., Goldhaber, M.B., 1997. Sulfur and carbon isotopes. In: Barnes, H.L. (Ed.), Geochemistry of Hydrothermal Ore Deposits, third ed. J Wiley and Sons, New York, pp. 517–611.
Oliver, N.H.S., Cleverley, J.S., Mark, G., Pollard, P.J., Fu, B., Marshall, L.J., Rubenach, M.J., Williams, P.J., Baker, T., 2004. Modeling the role of sodic alteration in the genesis of iron oxide-copper-gold deposits, Eastern Mount Isa block, Australia. Econ. Geol. 99, 1145–1176.
Pollard, P.J., 2006. An intrusion-related origin for Cu-Au mineralization in iron oxide-copper-gold (IOGG) provinces. Miner. Deposita 41, 179–187.
Polliand, M., Schaltegger, U., Frank, M., Fontbote, L., 2005. Formation of intra-arc volcanosedimentary basins in the western flank of the central Peruvian Andes during Late Cretaceous oblique subduction: field evidence and constraints from U-Pb ages and Hf isotopes. Int. J. Earth Sci. 94, 231–242.
Price, B.J., 1972. Minor Elements in Pyrites from the Smithers Map Area, bc and Exploration Applications of Minor Element Studies. University of British Columbia.
Rowins, S.M., Groves, D.I., McNaughton, N.J., Palmer, M.R., Eldridge, C.S., 1997. A reinterpretation of the role of granitoids in the genesis of neoproterozoic gold mineralization in the Telfer dome, western Australia. Econ. Geol. Bull. Soc. Econ. Geol. 92, 133–160.
Rye, R.O., Ohmoto, H., 1974. Sulfur and carbon isotopes and ore genesis - review. Econ. Geol. 69, 826–842.

Schlegel, T.U., Wagner, T., Boyce, A., Heinrich, C.A., 2017. A magmatic source of hydrothermal sulfur for the Prominent Hill deposit and associated prospects in the Olympic iron oxide copper-gold (IOCG) province of South Australia. Ore Geol. Rev. 89, 1058–1090.

Scott, R.J., Meffre, S., Woodhead, J., Gilbert, S.E., Berry, R.F., Emsbo, P., 2009. Development of framboidal pyrite during diagenesis, low-grade regional metamorphism, and hydrothermal alteration. Econ. Geol. 104, 1143–1168.

Seal, R.R., 2006. Sulfur isotope geochemistry of sulfide minerals. Rev. Mineral.Geochem 61, 633–677.

Sillitoe, R.H., 2003. Iron oxide-copper-gold deposits: an Andean view. Miner. Deposita 38, 787–812.

Ullrich, T.D., Clark, A., Kyser, T., 2001. The Candelaria Cu-Au deposit, III Region, Chile: product of long-term mixing of magmatic-hydrothermal and evaporite-sourced fluids GSA Annual Meeting, Boston, Abstracts with Programs, p A-3.

Ulrich, T., Long, D.G.F., Kamber, B.S., Whitehouse, M.J., 2011. In situ trace element and sulfur isotope analysis of pyrite in a paleoproterozoic gold placer deposit, Pardo and clement townships, Ontario, Canada. Econ. Geol. 106, 667–686.

Vidal, C.E., Injoqueespinoza, J., Sidder, G.B., Mukasa, S.B., 1990. Amphibolitic Cu-Fe skarn deposits in the central coast of Peru. Econ. Geol. Bull. Soc. Econ. Geol. 85, 1447–1461.

Wagner, T., Okrusch, M., Weyer, S., Lorenz, J., Lahaye, Y., Taubald, H., Schmitt, R.T., 2010. The role of the Kupferschiefer in the formation of hydrothermal base metal mineralization in the Spessart ore district, Germany: insight from detailed sulfur isotope studies. Miner. Deposita 45, 217–239.

Wasteneys, H.A., Clark, A.H., Farrar, E., Langridge, R.J., 1995. Grenvillian granulite-facies metamorphism in the arequipa massif, Peru – a Laurentia-Gondwana Link. Earth Planet. Sci. Lett. 132, 63–73.

Williams, P.J., Barton, M.D., Johnson, D.A., Fontboté, L., De Haller, A., Mark, G., Oliver, N.H., Marschik, R., 2005. Iron oxide copper-gold deposits: Geology, space-time distribution, and possible modes of origin. Econ Geol. 371–405.

Zhao, X.F., Zhou, M.F., 2011. Fe-Cu deposits in the Kangdian region, SW China: a Proterozoic IOCG (iron-oxide-copper-gold) metallogenic province. Miner. Deposita 46, 731–747. https://doi.org/10.1007/s00126-011-0342-y.

Zheng, Y., Zhang, L., Chen, Y.J., Hollings, P., Chen, H.Y., 2013. Metamorphosed Pb-Zn-(Ag) ores of the Keketale VMS deposit, NW China: Evidence from ore textures, fluid inclusions, geochronology and pyrite compositions. Ore Geol. Rev. 54, 167–180.